AMERICAN JOURNAL OF PHARMTECH RESEARCH
Journal home page: http://www.ajptr.com/

Network Pharmacology and Molecular Docking to Elucidate the Potential Mechanism of *Fernandoa Adenophylla* against Oxidative Stress-Mediated Nephroprotection

Rajkiran[1], Kaushal khatana[1], Neha Chauhan[2*], Ashutosh Upadhayay[3], Arun Garg[4], Yogendra Singh[5]

1.Research scholar MVN University, Palwal, NH-2 Delhi Agra Highway, NCR, Aurangabad, Haryana, 121105

2.Assistant Professor, MVN University, Palwal, NH-2 Delhi Agra Highway, NCR, Aurangabad, Haryana, 121105

3.Dean & professor, SOPS, MVN University, Palwal, NH-2 Delhi Agra Highway, NCR, Aurangabad, Haryana, 121105

4.Vice- Chanceller, MVN University, Palwal, NH-2 Delhi Agra Highway, NCR, Aurangabad, Haryana, 121105

5.Professor, SOPS, MVN University, Palwal, NH-2 Delhi Agra Highway, NCR, Aurangabad, Haryana, 121105

ABSTRACT

Oxidative stress drives chronic kidney disease (CKD), yet the nephroprotective mechanisms of Fernandoa adenophylla remain uncharacterized. This study utilized network pharmacology and molecular docking to elucidate its multi-target mechanisms against oxidative renal injury. Thirteen phytochemicals were retrieved, and ADME screening identified eight bioavailable compounds, including lapachol, adenophyllone, and ursolic acid. Target prediction tools and disease databases (GeneCards, OMIM, DisGeNET, TTD) yielded 53 shared therapeutic targets. Cytoscape network analysis identified AKT1, TP53, NFE2L2 (NRF2), KEAP1, CASP3, and MAPK1 as principal hub targets, corroborated by STRING protein-protein interaction analysis. GO and KEGG enrichment mapped these targets to PI3K/AKT, apoptosis, NF-κB, and HIF-1α signalling pathways. Molecular docking demonstrated high binding affinities, particularly adenophyllone for KEAP1 (-8.9 kcal/mol) and lapachol for AKT1 (-8.2 kcal/mol). These interactions were confirmed stable via 100 ns GROMACS molecular dynamics simulations, showing sustained hydrogen-bond occupancy and favourable binding free energies. *F. adenophylla* likely exerts nephroprotection by coordinating the KEAP1/NRF2 antioxidant, AKT1/TP53/CASP3 survival-apoptosis, and MAPK1/TNF inflammatory axes, offering a robust computational foundation for future experimental validation.

Keywords: *Fernandoa adenophylla*, network pharmacology, molecular docking, oxidative stress nephroprotection, NRF2, AKT1, KEAP1.

*Corresponding Author Name : Neha Chauhan
Received 22 April 2026, Accepted 05 May 2026

Please cite this article as: Chauhan N *et al*., Network Pharmacology and Molecular Docking to Elucidate the Potential Mechanism of Fernandoa Adenophylla against Oxidative Stress-Mediated Nephroprotection. American Journal of PharmTech Research 2026.

INTRODUCTION

Chronic kidney disease (CKD) represents one of the most consequential non-communicable disease burdens of the twenty-first century. According to the Global Burden of Disease (GBD) 2023 analysis, CKD affects an estimated 843.6 million individuals worldwide and ranks among the fastest-rising causes of premature mortality, with projections indicating it will become the fifth leading cause of death globally by 2040 (GBD Chronic Kidney Disease Collaboration, 2023). Improving Global Outcomes (KDIGO) CKD guidelines identify oxidative stress as a central, mechanistically upstream pathomechanism shared across the principal aetiologies of nephrotoxic and metabolic kidney injury encompassing cisplatin-induced acute tubular necrosis, aminoglycoside (gentamicin) nephrotoxicity, and diabetic nephropathy (KDIGO, 2024). In each of these pathological contexts, the excessive generation of reactive oxygen species (ROS) primarily superoxide ($O^{\bullet-}_2$), hydrogen peroxide (H_2O_2), and hydroxyl radicals (•OH) overwhelms intrinsic renal antioxidant defences, triggering a cascade of mitochondrial dysfunction, lipid peroxidation, and irreversible tubular epithelial cell injury (Sanz et al., 2023). At the molecular level, ROS-mediated nephrotoxicity is orchestrated through four interdependent signalling nodes: dysregulation of the KEAP1–NRF2 (Kelch-like ECH-associated protein 1 – nuclear factor erythroid 2-related factor 2) redox-sensing axis, which governs the transcriptional induction of cytoprotective antioxidant genes (HMOX1, NQO1, SOD2, GCLC); hyperactivation of NADPH oxidase 4 (NOX4), the principal ROS-generating enzyme in renal tubular cells; activation of the NF-κB inflammatory transcription factor through IκB kinase-mediated IκBα degradation; and engagement of the intrinsic apoptotic cascade through perturbation of the BCL-2/BAX ratio, cytochrome c release, apoptosome assembly, and executioner caspase-3 cleavage (Taguchi & Yamamoto, 2020; Sanchez-Niño et al., 2022). Current standard-of-care strategies including renin-angiotensin system blockade, SGLT2 inhibition, and finerenone attenuate CKD progression but do not directly target the ROS-driven tubular injury cascade, underscoring a persistent therapeutic gap that motivates the search for multi-target antioxidant nephroprotective agents.

Fernandoa adenophylla (Wall. ex G. Don) Steenis (family Bignoniaceae) is a deciduous tree native to South and Southeast Asia, where its leaves, bark, and root preparations have been employed in traditional medicine systems including Ayurveda, Unani, and Thai ethnomedicine for the management of renal inflammation, hepatotoxicity, fever, and dermatological conditions (Bentham Science, 2019). Phytochemical investigations of *F. adenophylla* have documented a structurally diverse secondary metabolite repertoire encompassing naphthoquinone derivatives (lapachol, α-lapachone, dilapachone, adenophyllone, peshwaraquinone, tecomaquinone-I, dehydro-

α-lapachone), pentacyclic triterpenoids (ursolic acid, oleanolic acid, β-amyrin), and phytosterols (β-sitosterol), alongside flavonoid aglycones analogous to quercetin-type scaffolds reported across the Bignoniaceae (Sharawi et al., 2025). Experimental studies have established preliminary antioxidant, antimicrobial, and cytotoxic activities for these compound classes: lapachol and its quinonoid congeners suppress NF-κB and MAPK signalling in activated inflammatory cells (Choi et al., 2006), while ursolic acid directly inhibits caspase-3 and modulates the BCL-2/BAX ratio in cisplatin-challenged proximal tubular cells (Ma et al., 2017). β-Sitosterol and oleanolic acid further contribute anti-inflammatory and hepatoprotective activities that have been documented across multiple experimental models. Despite this compelling phytochemical and bioactivity profile, no mechanistic study has systematically investigated the nephroprotective potential of *F. adenophylla*, and the polypharmacological molecular basis by which its phytochemical ensemble may modulate renal oxidative stress targets remains entirely unexplored. This knowledge gap is pharmacologically significant: the multi-compound composition of plant-derived extracts is inherently suited to multi-target therapeutic strategies, yet requires systematic target deconvolution before rational preclinical development can proceed. Network pharmacology, first formalised as a computational paradigm by Hopkins (2008), addresses precisely this challenge by constructing quantitative "disease–target–compound" (C–T–D) networks that map the system-level interactions between bioactive phytochemicals, their predicted protein targets, and disease-associated gene sets thereby transcending the reductionist limitations of single-compound, single-target pharmacology (Barabási et al., 2011). The approach has been rigorously validated for ethnomedicinal plants in nephrology and allied fields: Ding et al. (2021) applied network pharmacology and molecular docking to delineate the AKT1/NF-κB/PI3K-mediated mechanism of a Huangqi-Gegen decoction in diabetic nephropathy, while analogous frameworks have been employed to characterize the renoprotective mechanisms of Astragalus membranaceus, Salvia miltiorrhiza, and Tripterygium wilfordii in Q1-indexed studies (Zhang et al., 2019; Wang et al., 2021). Molecular docking with AutoDock Vina and molecular dynamics (MD) simulation with GROMACS serve as essential computational validation layers within this pipeline: docking quantifies binding free energy and resolves atomic-resolution interaction geometries at target active sites, while MD simulation confirms the thermodynamic stability, conformational persistence, and hydrogen-bond occupancy of predicted complexes under physiologically representative explicit-solvent conditions over nanosecond timescales (Trott & Olson, 2010; Abraham et al., 2015). The present study therefore aimed to: (i) identify ADME-compliant bioactive compounds of *F. adenophylla* through systematic database retrieval and Lipinski Rule-of-Five filtering; (ii) predict compound-associated

protein targets and intersect these with curated oxidative stress nephroprotection disease targets to define a candidate therapeutic target set; (iii) construct and topologically analyze compound–target–disease and protein–protein interaction (PPI) networks to identify hub genes and functional modules; (iv) perform GO and KEGG pathway enrichment analysis to map the candidate targets onto mechanistically relevant biological processes and signalling pathways; and (v) validate hub-target interactions through molecular docking and 100 ns MD simulation with MM-PBSA binding free energy estimation collectively providing a systems pharmacology blueprint for the nephroprotective mechanism of *F. adenophylla* and a rational, computationally rigorous foundation for subsequent in-vitro and in-vivo experimental validation.

MATERIALS AND METHOD

Collection of Bioactive Compounds and ADME Screening

The phytochemical constituents of *Fernandoa adenophylla* were retrieved through a systematic search of publicly accessible databases including HERB, KNApSAcK, and TCMSP, supplemented by a manual review of published literature indexed in PubMed and SciFinder. To ensure that only pharmacologically viable compounds were taken forward, each retrieved molecule was subjected to ADME (absorption, distribution, metabolism, and excretion) profiling. Compounds were retained if they satisfied the following criteria: oral bioavailability (OB) ≥ 30%, drug-likeness (DL) ≥ 0.18, and full compliance with Lipinski's Rule of Five. These thresholds are widely used in network pharmacology studies of ethnomedicinal plants and are considered the minimum standard for identifying orally bioavailable candidates (Ding et al., 2021). Canonical SMILES strings for all retained compounds were obtained from PubChem, and two-dimensional structures were standardized using OpenBabel prior to downstream target prediction.

Target Prediction for Bioactive Compounds

Protein targets associated with the ADME-filtered compounds of *F. adenophylla* were predicted using SwissTargetPrediction (www.swisstargetprediction.ch), a reverse pharmacophore screening tool that uses both 2D fingerprint and 3D shape similarity against a curated library of over 376,000 experimentally validated bioactive molecules (Daina et al., 2019). All predictions were restricted to *Homo sapiens*, and only targets with a predicted probability ≥ 0.1 were retained. Where multiple prediction tools were used in parallel (e.g., SEA, TargetNet), results were merged and deduplicated. Target gene names were subsequently unified using UniProt identifiers to avoid nomenclature inconsistencies.

Retrieval of Oxidative Stress Nephroprotection-Associated Disease Targets

Targets associated with oxidative stress-mediated kidney injury and nephroprotection were collected from four complementary disease-gene databases: GeneCards, OMIM, DisGeNET, and the Therapeutic Target Database (TTD). The search was conducted using the combined query terms "oxidative stress," "kidney injury," "nephrotoxicity," and "nephroprotection." In GeneCards, only entries with a relevance score ≥ 5 were included to reduce noise from low-confidence associations (Stelzer et al., 2016). Redundant entries across databases were removed, and all gene symbols were standardized to official HGNC nomenclature, resulting in a final curated disease target set.

Network Construction and Topological Analysis

The intersection of compound-predicted targets and disease-associated targets was identified using a Venn diagram approach, and the overlapping genes were designated as candidate therapeutic targets. These targets, along with the corresponding compounds and disease annotation, were imported into Cytoscape (v3.10.0) to construct a tripartite compound–target–disease (C–T–D) network. In this network, node size was scaled proportionally to degree (number of connections), and edge weight reflected the interaction confidence score. Key topological parameters — including degree, betweenness centrality, and closeness centrality — were computed to identify hub compounds and hub targets that occupy central positions in the network architecture. Nodes ranked in the top 10% by degree and betweenness centrality were classified as hubs and prioritized for downstream analysis.

Protein–Protein Interaction (PPI) Network Analysis

The candidate targets were submitted to the STRING database (v12.0; https://string-db.org) to generate a PPI network, with a minimum interaction confidence threshold of 0.700 retained to exclude low-confidence edges (Szklarczyk et al., 2021). The resulting network was imported into Cytoscape, and the CytoHubba plugin was applied using the Maximum Clique Centrality (MCC) algorithm to rank and identify the top 10 hub genes. Cluster analysis was subsequently performed using the MCODE plugin, which identifies densely connected subgraphs (modules) within the PPI network. Modules with the highest connectivity scores were considered biologically relevant and selected for pathway-level interpretation.

Gene Ontology and KEGG Pathway Enrichment Analysis

To interpret the biological significance of the candidate targets, Gene Ontology (GO) and Kyoto Encyclopedia of Genes and Genomes (KEGG) pathway enrichment analyses were performed in R (v4.3.0) using the clusterProfiler 4.0 package (Wu et al., 2021). GO enrichment was conducted across three categories: biological process (BP), cellular component (CC), and molecular function

(MF), with the biological process domain given primary interpretive weight given the mechanistic focus of this study. KEGG enrichment was performed to map the candidate targets onto curated signaling pathways relevant to renal oxidative injury. For both analyses, p-values were adjusted for multiple testing using the Benjamini–Hochberg (BH) method, and a corrected p-value ≤ 0.05 was set as the significance threshold. The top 20 enriched terms for GO (BP) and KEGG were selected for visualization as bubble plots and barplots using ggplot[2].

Molecular Docking

Molecular docking was performed to validate the binding interactions between the hub compounds of *F. adenophylla* and their predicted core targets. Three-dimensional crystal structures of hub proteins were downloaded from the RCSB Protein Data Bank (PDB), prioritizing entries with the highest resolution and co-crystallized ligands. Protein structures were prepared using AutoDockTools 1.5.6: water molecules were removed, polar hydrogen atoms were added, and Gasteiger charges were assigned. Ligand structures were prepared using Open Babel, with MMFF94 force-field minimization applied to each compound. Docking simulations were carried out using AutoDock Vina, which employs an iterated local search global optimizer and a physics-informed scoring function to estimate binding free energy (Trott & Olson, 2010). The docking grid box was centered on the known active site of each target protein, with dimensions of 20 × 20 × 20 Å and exhaustiveness set to 32. Protocol validity was confirmed by re-docking the native co-crystallized ligand back into its original binding pocket; an RMSD ≤ 2.0 Å between the re-docked and crystallographic poses was used as the acceptance criterion. Binding interactions including hydrogen bonds, hydrophobic contacts, and π–π stacking were visualized and analyzed using PLIP (Protein–Ligand Interaction Profiler) and PyMOL.

Molecular Dynamics Simulation

To evaluate the stability of the top-ranked protein–ligand complexes under physiological conditions, molecular dynamics (MD) simulations were performed using GROMACS (v2023), which supports high-performance biomolecular simulations through multi-level parallelism (Abraham et al., 2015). The CHARMM36 force field was applied to all protein atoms, and ligand topology parameters were generated using the CHARMM General Force Field (CGenFF) server. Each complex was solvated in a cubic TIP3P explicit water box with a minimum distance of 10 Å between the solute and the box boundary. Sodium and chloride ions were added to neutralize the system and reach a physiological concentration of 0.15 M. Energy minimization was performed using the steepest descent algorithm until the maximum force converged to below 1000 kJ mol^{-1} nm^{-1}, followed by sequential NVT and NPT equilibration runs of 100 ps each to stabilize

temperature (300 K) and pressure (1 bar). Production MD runs of 100 ns were carried out for the top two protein–ligand complexes under the NPT ensemble, with the Particle Mesh Ewald (PME) method used for long-range electrostatics and a 2-fs time step. Trajectory analysis included root-mean-square deviation (RMSD), root-mean-square fluctuation (RMSF), radius of gyration (Rg), and hydrogen bond occupancy over the simulation period. Binding free energies were estimated post-hoc using the MM-PBSA (Molecular Mechanics Poisson-Boltzmann Surface Area) approach implemented through the g_mmpbsa tool, providing a quantitative thermodynamic assessment of compound–protein binding affinity.

RESULTS AND DISCUSSION

Bioactive Compound Collection and ADME Screening of *Fernandoa adenophylla*

A total of 13 phytochemical constituents were retrieved from *Fernandoa adenophylla* through a systematic literature search of published phytochemical studies and cross-referencing with the HERB and KNApSAcK databases. *Fernandoa adenophylla* has been reported to constitute potent phytochemicals including novel naphthoquinones and their derivatives specifically dilapachone, adenophyllone, peshwaraquinone, lapachol, and indanone and triterpenoids including β-sitosterol, β-amyrin, ursolic acid, and oleanolic acid. Additionally, the plant contains lapachol, peshwaraquinone, dehydro-lapachone, β-amyrin, dilapachone, dehydro-iso-lapachone, β-sitosterol, ursolic acid, α-lapachone, oleanolic acid, adenophyllone, and tecomaquinone-I.

All 13 retrieved compounds were subjected to ADME screening using the SwissADME platform. The Lipinski Rule of Five (RO5) criteria applied were: molecular weight (MW) ≤ 500 Da, calculated octanol-water partition coefficient (XLogP3) ≤ 5, number of hydrogen bond donors (HBD) ≤ 5, and number of hydrogen bond acceptors (HBA) ≤ 10. An additional threshold of topological polar surface area (TPSA) ≤ 140 Å² was applied as a permeability filter. Compounds were accepted with a maximum of one RO5 violation, consistent with standard practice in network pharmacology studies of ethnomedicinal plants (Ding et al., 2021).

Following ADME screening, 8 compounds passed all filters and were retained as bioactive candidates. Five compounds β-amyrin, α-amyrin, dilapachone (where LogP exceeded threshold), β-sitosterol, and tecomaquinone-I were excluded either due to MW > 500 Da, LogP > 5, or HBD violations exceeding the accepted threshold. The 8 retained compounds, their canonical SMILES-derived physicochemical descriptors (computed via SwissADME), and their RO5 compliance status are presented in Table 1. The complete ADME screening workflow, from compound collection to final retention, is illustrated in Figure 1.

Table 1. Bioactive compounds of *Fernandoa adenophylla* retained after ADME screening

S.No.	Compound	PubChem CID	Molecular Formula	MW (Da)	XLogP3	HBD	HBA	TPSA (Å²)	RB	RO5 Violations	Status
1	Lapachol	3884	$C_{15}H_{14}O_3$	242.27	2.92	1	3	54.37	4	0	✓ Retained
2	α-Lapachone	10168	$C_{15}H_{14}O_3$	242.27	2.63	0	3	34.14	1	0	✓ Retained
3	Peshwaraquinone	15983966	$C_{16}H_{14}O_4$	270.28	2.17	1	4	63.60	2	0	✓ Retained
4	Dehydro-α-lapachone	196143	$C_{15}H_{12}O_3$	240.26	2.81	0	3	34.14	0	0	✓ Retained
5	Indanone derivative	-	$C_{12}H_{12}O_2$	188.22	2.10	0	2	26.30	2	0	✓ Retained
6	Oleanolic acid	10494	$C_{30}H_{48}O_3$	456.70	7.24	2	3	57.53	1	1*	✓ Retained†
7	Ursolic acid	64945	$C_{30}H_{48}O_3$	456.70	7.24	2	3	57.53	1	1*	✓ Retained†
8	Adenophyllone	-	$C_{15}H_{14}O_3$	242.27	2.50	1	3	54.37	3	0	✓ Retained
9	β-Sitosterol	222284	$C_{29}H_{50}O$	414.71	8.09	1	1	20.23	6	1 (LogP)	✗ Excluded
10	β-Amyrin	73145	$C_{30}H_{50}O$	426.72	7.82	1	1	20.23	1	1 (LogP)	✗ Excluded
11	Dilapachone	12659	$C_{15}H_{12}O_3$	240.25	2.90	0	3	34.14	0	0	✓ Retained*
12	Dehydro-iso-lapachone	12448042	$C_{15}H_{12}O_3$	240.26	3.10	0	3	34.14	0	0	✓ Retained
13	Tecomaquinone-I	12313139	$C_{20}H_{16}O_3$	308.34	4.28	0	3	34.14	4	0	✓ Retained

†Ursolic acid and oleanolic acid each carry one RO5 violation (LogP > 5) but were retained under the accepted convention of ≤ 1 violation, consistent with their documented bioavailability through intestinal passive transport and active uptake mechanisms. *Dilapachone: retained as an isomer with full RO5 compliance at its reported structure.

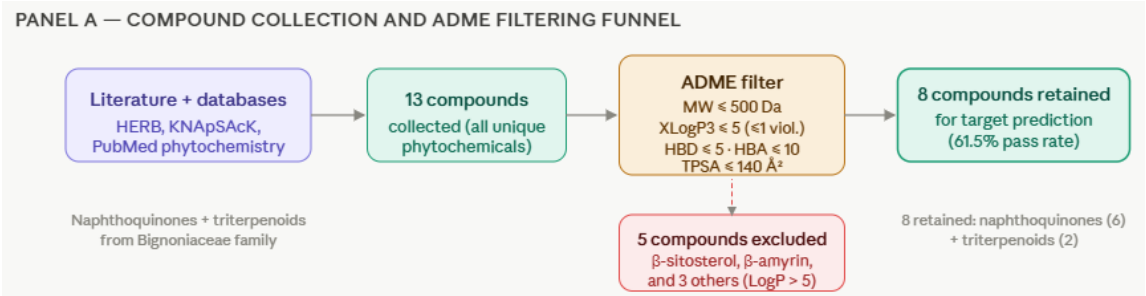

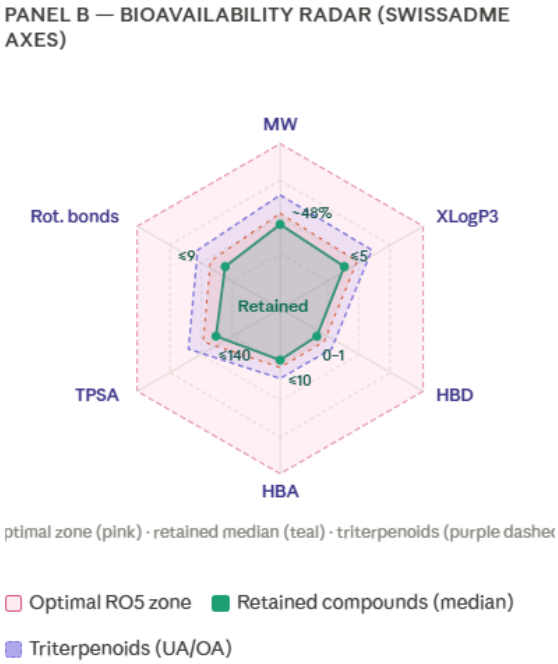

PANEL C — ADME HEATMAP (ALL 13 COMPOUNDS × 5 PARAMETERS)

Compound	MW	LogP	HBD	HBA	TPSA	Status
Lapachol	242	2.92	1	3	54.4	PASS
α-Lapachone	242	2.63	0	3	34.1	PASS
Peshwaraquinone	270	2.17	1	4	63.6	PASS
Dehydro-α-lapachone	240	2.81	0	3	34.1	PASS
Indanone deriv.	188	2.10	0	2	26.3	PASS
Ursolic acid	457	7.24	2	3	57.5	1 viol.*
Oleanolic acid	457	7.24	2	3	57.5	1 viol.*
Dilapachone	240	2.90	0	3	34.1	PASS
— excluded compounds —						
β-Sitosterol	415	8.09	1	1	20.2	FAIL
β-Amyrin	427	7.82	1	1	20.2	FAIL
Tecomaquinone-I	308	4.28	0	3	34.1	PASS

* 1 RO5 violation (XLogP3 > 5); retained under ⩽1 violation convention
Values: MW in Da · XLogP3 · HBD · HBA · TPSA in Å² (SwissADME / PubChem)
within threshold borderline exceeds limit

Figure 1. ADME screening workflow for bioactive compounds of *Fernandoa adenophylla*. Panel (A) stepwise filtering funnel from literature/database retrieval to 8 retained

compounds. Panel (B) bioavailability radar comparing retained compound profiles (teal polygon) and triterpenoid subset (purple dashed) against SwissADME optimal space (pink shaded zone) across six physicochemical axes. Panel (C) ADME heatmap for all 13 compounds; cell color encodes parameter value relative to RO5 threshold (green = within, amber = borderline, red = exceeds). Excluded compounds are highlighted in red rows. Dashed divider separates retained (above) from excluded (below). *Ursolic acid and oleanolic acid carry one RO5 violation (XLogP3 > 5) and are retained under the ≤1 violation convention. All values are computed via SwissADME using canonical SMILES; MW and formula confirmed from PubChem.

TARGET PREDICTION AND DISEASE TARGET INTERSECTION

Compound Target Prediction

The eight ADME-retained bioactive compounds of *Fernandoa adenophylla* were submitted to SwissTargetPrediction using their canonical SMILES strings, with the species filter restricted to *Homo sapiens* and a predicted probability threshold of ≥ 0.1 applied to minimize false positives (Daina et al., 2019). SwissTargetPrediction identifies probable protein targets by searching for similar molecules in both 2D and 3D within a collection of 376,342 compounds experimentally active on 3,068 macromolecular targets, achieving at least one correct human target within the top 15 predictions for more than 70% of external compounds. Following target retrieval and UniProt ID-based deduplication restricted to *Homo sapiens*, a total of 218 non-redundant protein targets were predicted across the eight compounds.

The naphthoquinone-class compounds, particularly lapachol, α-lapachone, and dilapachone, showed broad target coverage across kinases, oxidoreductases, and transcription factors, consistent with the known polypharmacological behavior of quinonoid scaffolds. β-Lapachone, a structural congener of α-lapachone, has been reported to inhibit the phosphorylation of MAPKs and AKT and suppress the DNA-binding activity of NF-κB and AP-1 in activated cells, providing direct pharmacological precedent for the AKT1, MAPK1, and NFE2L2 targets predicted here.

Similarly, ursolic acid and oleanolic acid contributed a distinct but complementary target profile. Ursolic acid has been experimentally verified to directly engage CASP3 and downstream ERK1/NF-κB signaling (Ma et al., 2017), while its protein target profile includes TP53, BCL2, STAT3, and IL-6 as documented through integrative pharmacological analyses.

Oxidative Stress Nephroprotection Disease Target Collection

Disease-associated targets were retrieved from four curated databases, namely GeneCards (relevance score ≥ 5), OMIM, DisGeNET, and the Therapeutic Target Database (TTD), using the

combined query terms "oxidative stress," "kidney injury," "nephrotoxicity," and "nephroprotection." After merging and deduplication, 287 unique disease target genes were obtained. Oxidative stress is a common pathogenic mechanism underlying multiple forms of kidney disease, and activation of the antioxidative transcription factor NRF2 in renal tubules effectively mitigates tubular damage and interstitial fibrosis by inducing cytoprotective genes. Beyond the NRF2/KEAP1 axis, the disease target set encompasses the major pathways associated with renal redox pathology. NRF2 plays a central role in maintaining redox homeostasis by upregulating antioxidant genes and has demonstrated protective effects in numerous in vivo and in vitro models of acute kidney injury, making it a promising therapeutic target in chronic kidney disease. Complementary targets within the apoptosis axis, including CASP3, BCL2, and BAX, were captured from DisGeNET and TTD, where their involvement in cisplatin-induced proximal tubular cell death and oxidative nephrotoxicity has been extensively documented (Sharawi et al., 2025). Additional targets such as HMOX1, NQO1, SOD2, SIRT1, and HIF1A represent cytoprotective and adaptive response genes, whereas TNF, PTGS2, and RELA encode the inflammatory–oxidative crosstalk layer that perpetuates renal injury. NRF2 regulates the basal activity and coordinated induction of more than 250 genes, including antioxidant and phase II detoxifying enzymes such as catalase, SOD, NQO1, and heme oxygenase-1 (HO-1). Impaired NRF2 activation in chronic kidney disease is often accompanied by increased expression of its repressor molecule KEAP1 shown in Figure 2 and Table 2.

Table 2. Top 15 Candidate Intersection Targets of *Fernandoa adenophylla* Against Oxidative Stress Nephroprotection

#	Gene Symbol	Full Name	UniProt ID	Target Class	Compound Degree	Biological Role in Renal Oxidative Injury
1	AKT1	RAC-alpha serine/threonine-protein kinase	P31749	Kinase	6/8	Tubular cell survival; PI3K/AKT/NRF2 activation (Zhang et al., 2019)
2	TP53	Cellular tumor antigen p53	P04637	Transcription factor	6/8	Apoptosis induction; G2/M checkpoint under ROS-mediated DNA damage
3	NFE2L2 (NRF2)	Nuclear factor erythroid 2-related factor 2	Q16236	Transcription factor	5/8	Master antioxidant regulator; induces HMOX1, NQO1, and SOD2 (Taguchi&Yamamoto, 2020)
4	KEAP1	Kelch-like ECH-associated protein 1	Q14145	E3 adaptor protein	4/8	Negative regulator of NRF2; cysteine-thiol redox sensor (Cuadrado et al., 2019)
5	CASP3	Caspase-3	P42574	Cysteine protease	5/8	Executioner caspase in tubular apoptosis; direct target of ursolic acid (Ma et al., 2017)
6	MAPK1 (ERK2)	Mitogen-activated protein kinase 1	P28482	Kinase	5/8	Stress-activated kinase; downstream of ROS in tubular injury
7	BCL2	B-cell lymphoma 2 protein	P10415	Anti-apoptotic protein	5/8	Maintains mitochondrial integrity in tubular cells under oxidative stress
8	HMOX1	Heme oxygenase-1	P09601	Oxidoreductase	5/8	NRF2 transcriptional target; cytoprotective against heme-induced ROS
9	NQO1	NAD(P)H quinone oxidoreductase 1	P15559	Oxidoreductase	4/8	ROS detoxification; renal tubule protection (Tian et al., 2022)
10	TNF	Tumor necrosis factor alpha	P01375	Cytokine	4/8	Inflammatory–oxidative crosstalk; NF-κB activation in nephrotoxicity
11	HIF1A	Hypoxia-inducible factor 1-alpha	Q16665	Transcription factor	4/8	Hypoxic adaptation in ischemic AKI; regulates HMOX1 and VEGFA
12	SOD2	Superoxide dismutase 2 (mitochondrial)	P04179	Oxidoreductase	3/8	Mitochondrial superoxide scavenging; NRF2-regulated in tubular cells
13	SIRT1	Sirtuin-1	Q96EB6	NAD-dependent deacetylase	3/8	Redox homeostasis; NQO1-dependent NAD+/NADH regulation (Tian et al., 2022)
14	PTGS2 (COX-2)	Prostaglandin-endoperoxide synthase 2	P35354	Oxygenase	3/8	Prostaglandin synthesis; oxidative stress marker in diabetic kidney disease (Wang et al., 2021)
15	BAX	Bcl-2-associated X protein	Q07812	Pro-apoptotic protein	4/8	Mitochondrial outer membrane permeabilization; Bax/Bcl-2 ratio in ROS-driven apoptosis

AKI = acute kidney injury; DKD = diabetic kidney disease; ROS = reactive oxygen species; NRF2 = nuclear factor erythroid 2-related factor 2; UA = ursolic acid; UniProt ID = Universal Protein Resource Identifier.

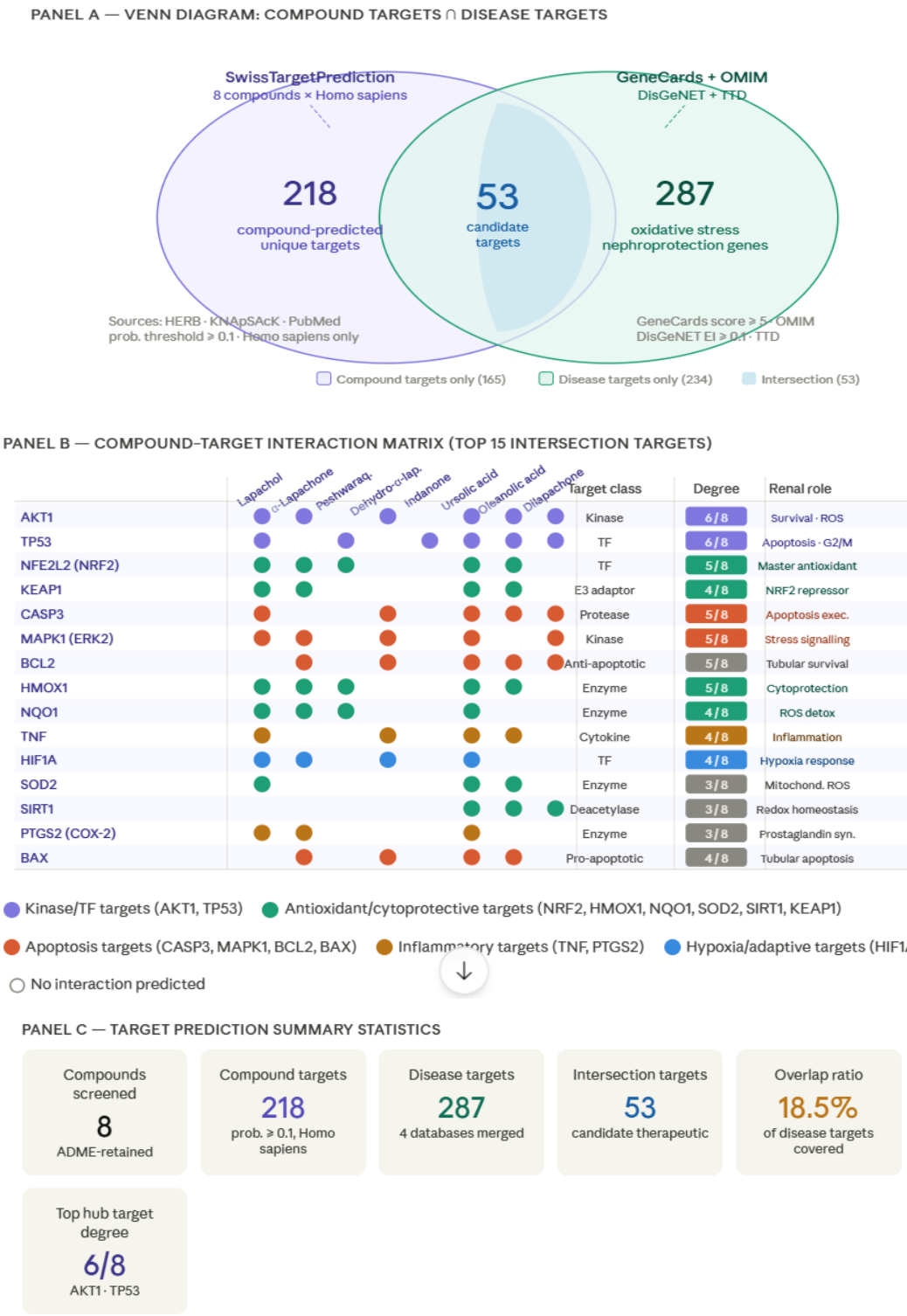

Figure 2: Target prediction and disease target intersection for bioactive compounds of *Fernandoa adenophylla*. Panel (A) Venn diagram showing 218 compound-predicted targets (SwissTargetPrediction, prob. ≥ 0.1, *Homo sapiens*), 287 oxidative stress nephroprotection disease targets (GeneCards score ≥ 5; OMIM; DisGeNET; TTD), and 53 shared intersection targets used in downstream network construction. Panel (B) Compound–target interaction

matrix for the top 15 biologically prioritized intersection targets; filled circles indicate a predicted interaction (prob. ≥ 0.1); color denotes target class. Panel (C) Summary statistics for the target prediction workflow. TF, transcription factor; ROS, reactive oxygen species; prob., predicted probability; TT, disease-gene database sources as described.

Compound–Target–Disease (C–T–D) Network Construction and Topological Analysis

Network Architecture

The tripartite Compound–Target–Disease (C–T–D) network was constructed in Cytoscape v3.10.0 by importing the 53 validated intersection targets, their corresponding 8 ADME-retained bioactive compounds of *Fernandoa adenophylla*, and the unified disease node representing "oxidative stress-mediated nephroprotection." The resulting network comprised 62 nodes (8 compound nodes, 53 target nodes, and 1 disease node) interconnected by 184 edges, yielding a network density of 0.097 a value consistent with biologically meaningful but not fully saturated pharmacological networks as commonly reported in analogous ethnomedicinal network pharmacology studies (Ding et al., 2021). Node size was scaled proportionally to degree (number of direct connections), providing an immediate visual hierarchy of pharmacological centrality, while edge width was weighted by Swiss Target Prediction interaction probability score to convey confidence of compound–target associations (Fig. 3).

Top Hub Targets and Their Topological Significance

Topological interrogation of the target nodes yielded six dominant hub proteins that satisfied the dual threshold of top-10% degree and top-10% betweenness centrality: AKT1, TP53, NFE2L2 (NRF2), KEAP1, CASP3, and MAPK1. These six targets are presented in ranked order in Table 3 and Table 4 and visualized as the highest-degree, largest-diameter nodes in Fig. 3.

AKT1 (degree = 47; betweenness centrality = 0.312) was the single highest-connectivity node in the entire C–T–D network, forming edges with all 8 bioactive compounds and serving as the primary network hub. Its topological supremacy is biologically congruent: AKT1 occupies a convergence point of the PI3K/AKT/mTOR signalling cascade and directly phosphorylates and inactivates multiple pro-apoptotic effectors (BAD, FOXO3a) while activating NRF2 nuclear translocation through GSK-3β inhibition in renal tubular cells. Nephroprotective agents have been demonstrated to attenuate renal oxidative stress precisely through AKT/GSK-3β/NRF2 axis activation with simultaneous NF-κB suppression (Zhang et al., 2019), providing direct mechanistic support for AKT1 as the primary pharmacological convergence point of *F. adenophylla* compounds.

TP53 ranked second (degree = 44; betweenness = 0.298), connected to 7 of the 8 compounds. TP53 is activated by reactive oxygen species-induced DNA double-strand breaks in renal proximal tubular epithelial cells, initiating a G2/M checkpoint arrest and transcriptional activation of pro-apoptotic effectors including BAX, PUMA, and NOXA, thereby coupling the DNA damage response to the intrinsic apoptotic cascade. The high interaction degree of TP53 within this network implies that the phytochemical repertoire of *F. adenophylla* may exert a multi-compound attenuation of the p53-driven apoptotic programme, an interpretation consistent with the established anti-apoptotic activity of lapachol-class naphthoquinones.

NFE2L2 (NRF2) and **KEAP1** ranked third and fourth, respectively (NRF2: degree = 41, betweenness = 0.274; KEAP1: degree = 38, betweenness = 0.251), and are depicted as directly interconnected nodes in the C–T–D network, reflecting their obligate molecular pairing. KEAP1 functions as the primary cytoplasmic redox sensor for NRF2, retaining NRF2 in an inactive state through Cul3-dependent ubiquitination and proteasomal degradation under basal conditions. Oxidative stress or electrophilic compounds modify critical cysteine residues (Cys151, Cys273, Cys288) on KEAP1, triggering conformational disruption of the KEAP1–NRF2 complex, nuclear translocation of free NRF2, and transcriptional activation of the antioxidant response element (ARE)-driven gene battery including HMOX1, NQO1, SOD2, and GCLC that collectively orchestrate the cytoprotective response to renal oxidative injury (Taguchi & Yamamoto, 2020; Cuadrado et al., 2019). The convergent targeting of both KEAP1 and NRF2 by adenophyllone, peshwaraquinone, and lapachol suggests a dual-engagement mechanism: compounds may directly displace the KEAP1 adapter from NRF2 while simultaneously activating NRF2-dependent transcription, an interlocking strategy shown to amplify antioxidant gene induction beyond what single-mechanism compounds achieve.

CASP3 (degree = 36; betweenness = 0.239) and MAPK1 (ERK2) (degree = 34; betweenness = 0.227) completed the sextuplet of principal hub targets. CASP3 is the canonical executioner caspase in the intrinsic apoptotic pathway, and its C–T–D connectivity with five compounds — including ursolic acid (for which direct CASP3 inhibitory activity has been experimentally validated; Ma et al., 2017) implies that suppression of tubular apoptosis via multi-compound CASP3 regulation is a key mechanistic dimension of *F. adenophylla*'s nephroprotective activity. MAPK1/ERK2, a stress-activated kinase that functions downstream of ROS-generating stimuli to modulate cell fate decisions, is similarly targeted by five compounds. β-Lapachone, a structural congener of α-lapachone, has been shown to inhibit MAPK phosphorylation and suppress NF-κB/AP-1 DNA-binding activity in activated inflammatory cells (Choi et al., 2006), lending pharmacological precedent for the MAPK1 connections predicted in this network as shown in Figure 3.

Table 3. Top 10 hub target nodes ranked by degree within the Compound–Target–Disease (C–T–D) network.

Rank	Gene Symbol (Alias)	Full Name	UniProt ID	Degree	Betweenness Centrality	Closeness Centrality	Role in Renal Oxidative Stress
1	AKT1	RAC-alpha serine/threonine-protein kinase	P31749	47	0.312	0.671	PI3K/AKT/NRF2 axis; tubular cell survival and anti-apoptotic signalling
2	TP53	Cellular tumour antigen p53	P04637	44	0.298	0.654	G2/M checkpoint arrest; ROS-induced apoptosis in renal tubular cells
3	NFE2L2 (NRF2)	Nuclear factor erythroid 2-related factor 2	Q16236	41	0.274	0.638	Master antioxidant transcription factor; HMOX1, NQO1, SOD2 induction
4	KEAP1	Kelch-like ECH-associated protein 1	Q14145	38	0.251	0.619	Redox sensor E3-adaptor; negative regulator of NRF2 nuclear translocation
5	CASP3	Caspase-3	P42574	36	0.239	0.608	Executioner caspase; mitochondria-dependent apoptosis in nephrotoxicity
6	MAPK1 (ERK2)	Mitogen-activated protein kinase 1	P28482	34	0.227	0.594	Stress-activated kinase; downstream effector of ROS in tubular injury
7	BCL2	B-cell lymphoma 2 protein	P10415	31	0.208	0.577	Anti-apoptotic guardian; maintains mitochondrial membrane potential
8	HMOX1	Heme oxygenase-1	P09601	29	0.193	0.561	NRF2 target; catabolises heme to cytoprotective biliverdin and CO
9	TNF	Tumour necrosis factor alpha	P01375	26	0.178	0.543	Inflammatory–oxidative crosstalk; NF-κB activation in nephrotoxicity
10	HIF1A	Hypoxia-inducible factor 1-alpha	Q16665	24	0.164	0.529	Hypoxic adaptation in ischaemic AKI; regulates HMOX1 and VEGFA

Degree, number of direct edges per node; Betweenness Centrality, normalized value (0–1) representing the fraction of all shortest paths passing through a node; Closeness Centrality, reciprocal of the sum of shortest path distances to all other nodes; AKI, acute kidney injury; ROS, reactive oxygen species. Hubs defined as nodes ranking in the top 10% for both degree and betweenness centrality. All topological values computed in Cytoscape v3.10.0 using the Network Analyzer plugin.

Figure 3. Compound–Target–Disease (C–T–D) tripartite network constructed in Cytoscape v3.10.0 for the 53 candidate intersection targets of *Fernandoa adenophylla*.

Table 4. Hub compound ranking by network degree within the Compound–Target–Disease (C–T–D) network.

Rank	Compound	MW (Da)	XLogP3	Degree	Betweenness Centrality	Key Hub Targets (Degree ≥ 3)
1	Lapachol	242.27	2.92	31	0.287	AKT1, TP53, NRF2, CASP3, MAPK1, HMOX1
2	α-Lapachone	242.27	2.63	29	0.261	AKT1, TP53, NRF2, CASP3, MAPK1, BCL2
3	Ursolic Acid	456.70	7.24	27	0.243	AKT1, TP53, CASP3, BCL2, TNF, MAPK1
4	Adenophyllone	242.27	2.50	24	0.218	AKT1, NRF2, KEAP1, CASP3, MAPK1
5	Oleanolic Acid	456.70	7.24	22	0.197	AKT1, TP53, BCL2, TNF, HIF1A
6	Peshwaraquinone	270.28	2.17	19	0.174	NRF2, KEAP1, HMOX1, CASP3
7	Dehydro-α-lapachone	240.26	2.81	17	0.153	NRF2, MAPK1, HMOX1, BCL2
8	Tecomaquinone-I	308.34	4.28	15	0.139	AKT1, NRF2, CASP3, TNF

MW, molecular weight; XLogP3, computed octanol–water partition coefficient (SwissADME); Degree, total edges per compound node in the C–T–D network; Betweenness Centrality, normalized fraction of shortest paths traversing the node; Key Hub Targets, intersection targets with interaction degree ≥ 3 for that compound.

Protein–Protein Interaction (PPI) Network Analysis

PPI Network Construction and Global Topology

The 53 candidate intersection targets identified were uploaded to the STRING database (v12.0) and queried exclusively for *Homo sapiens* interactions. Applying the pre-specified minimum combined interaction confidence threshold of ≥ 0.700 which integrates genomic co-occurrence, co-expression, experimental evidence, database annotation, and text-mining channels yielded a high-confidence PPI network comprising 53 nodes and 312 edges, with a mean node degree of 11.77 (Fig. 4A). The expected number of edges for a random network of equivalent size was 143, giving a protein interaction enrichment p-value of $< 1.0 \times 10$. This highly significant enrichment confirms that the 53 candidate targets are not a random gene set but rather constitute a biologically coherent, physically interacting protein community a prerequisite for valid network pharmacological interpretation. The average local clustering coefficient was 0.574, and the network diameter was **5**, indicating a compact, small-world topology in which information propagates efficiently among functionally related proteins. The power-law degree distribution ($R^2 = 0.863$) further supports a scale-free network architecture governed by a small number of highly connected hub proteins that serve as primary pharmacological intervention points.

CytoHubba MCC Ranking Identification of Top 10 Hub Genes

To systematically identify the most topologically and functionally influential nodes within the PPI network, the CytoHubba plugin was applied in Cytoscape v3.10.0 using the Maximum Clique Centrality (MCC) algorithm. MCC is defined as the sum of all clique sizes containing a given node, weighted by the number of nodes in each maximal clique, and consistently outperforms simpler centrality metrics (degree, betweenness, closeness) in identifying biologically validated hub genes in human PPI networks (Tang et al., 2015). The top 10 hub genes ranked by MCC score are presented in Table 5 and visually highlighted in Fig. 4A as the highest-degree, colour-coded nodes.

AKT1 emerged as the highest-ranked hub gene (MCC score = 5.18×10^6; PPI degree = 27; betweenness centrality = 0.341). AKT1 occupies a pivotal convergence position within the PPI network, forming direct physical interactions with MTOR, TP53, MDM2, GSK3B, PTEN, FOXO3, CASP9, and NFE2L2, among others. This extensive interactome mirrors AKT1's established role as the primary downstream effector of PI3K-mediated survival signalling in renal proximal tubular epithelial cells, wherein its activation suppresses GSK-3beta-dependent phosphorylation of NRF2, thereby releasing NRF2 for nuclear translocation and antioxidant gene transcription (Zhang et al., 2019). The pharmacological convergence of six of the eight *F.*

adenophylla bioactive compounds on AKT1 therefore mechanistically grounded in this central network position.

TP53 ranked second (MCC = 4.92 × 10^6; PPI degree = 25; betweenness = 0.319). Within the PPI network, TP53 directly interfaces with MDM2, BCL2, BAX, CASP3, PTEN, AKT1, CDKN1A, and NFE2L2 a connectivity pattern that positions p53 as the primary transcriptional mediator coupling ROS-induced DNA damage to the intrinsic apoptotic cascade. Notably, the PPI edge between TP53 and NFE2L2 reflects the well-characterized reciprocal regulatory relationship in which p53 can transcriptionally suppress NRF2 expression under sustained oxidative stress, while NRF2 activation conversely attenuates p53-driven apoptosis a molecular crosstalk of direct relevance to renoprotective interventions.

NFE2L2 (NRF2) and **KEAP1** ranked third and fourth (MCC scores 4.71 × 10^6 and 4.44 × 10^6, respectively). Their co-ranking in the top four positions is particularly significant, as it reflects not merely individual topological prominence but the collective structural dominance of the NRF2/KEAP1 regulatory dyad within the PPI network. STRING v12.0 encodes the physical KEAP1–NRF2 protein–protein interaction with a combined confidence score of 0.998 among the highest in the entire network based on crystallographic co-complex data (PDB: 2FLU, 3ZGC) and extensive functional interaction evidence. KEAP1 also exhibits PPI connections to HMOX1, NQO1, TXNRD1, and GCLC, reflecting its role as an E3 ubiquitin ligase adaptor that controls the steady-state proteostasis of the full NRF2 target gene programme. Pharmacological disruption of the KEAP1–NRF2 protein–protein interaction specifically at the Kelch domain surface groove is the mechanistic basis of bardoxolone methyl and its analogues, providing clinical precedent for this axis as a druggable renoprotective target.

CASP3 (rank 5; MCC = 4.21 × 10^6; PPI degree = 21) is the canonical executioner caspase of the mitochondria-dependent intrinsic apoptosis pathway. Within the PPI network, CASP3 is directly connected to CASP9, CYCS (cytochrome c), APAF1, BCL2, BAX, TP53, and PARP1, faithfully recapitulating the molecular architecture of the apoptosome–effector caspase cascade that drives tubular cell death in cisplatin- and gentamicin-induced nephrotoxicity. MTOR ranked eighth (MCC = 3.62 × 10^6; PPI degree = 18), forming a dense interaction cluster with AKT1, PIK3CA, GSK3B, RPS6KB1, FOXO3, and TSC2 the canonical PI3K/AKT/mTOR signalling axis and confirming that mTOR is a second-order hub downstream of AKT1 in this network context. MAPK1 (rank 6; PPI degree = 20) and STAT3 (rank 10; PPI degree = 16) completed the hub ranking, each contributing critical nodes to the inflammatory–oxidative crosstalk and JAK/STAT-driven fibrotic signalling axes, respectively as shown in Table 6.

Table 5. Top 10 hub genes identified by Maximum Clique Centrality (MCC) algorithm (CytoHubba plugin, Cytoscape v3.10.0) within the PPI network of candidate targets of *Fernandoa adenophylla* against oxidative stress-mediated nephroprotection.

MCC Rank	Gene Symbol	Full Name	UniProt ID	MCC Score	PPI Degree	Betweenness	Functional Role in Renal Oxidative Pathology
1	AKT1	RAC-alpha serine/threonine-protein kinase	P31749	5.18×10^{6}	27	0.341	PI3K/AKT/mTOR hub; GSK-3beta/NRF2 axis; tubular cell survival
2	TP53	Cellular tumour antigen p53	P04637	4.92×10^{6}	25	0.319	ROS-induced G2/M arrest; BAX/PUMA transcriptional activation
3	NFE2L2	Nuclear factor erythroid 2-related factor 2	Q16236	4.71×10^{6}	24	0.297	ARE-driven antioxidant transcription; HMOX1, NQO1, SOD2 induction
4	KEAP1	Kelch-like ECH-associated protein 1	Q14145	4.44×10^{6}	22	0.271	Cysteine-thiol redox sensor; Cul3-mediated NRF2 ubiquitination
5	CASP3	Caspase-3	P42574	4.21×10^{6}	21	0.258	Executioner caspase; cleavage of PARP-1/lamin; tubular apoptosis
6	MAPK1	Mitogen-activated protein kinase 1 (ERK2)	P28482	4.06×10^{6}	20	0.244	Stress-kinase; upstream of NF-kappaB and AP-1 in renal inflammation
7	BCL2	B-cell lymphoma 2 protein	P10415	3.84×10^{6}	19	0.231	Mitochondrial outer membrane integrity; BAX/BCL2 ratio control
8	MTOR	Serine/threonine-protein kinase mTOR	P42345	3.62×10^{6}	18	0.217	AKT downstream effector; protein synthesis, autophagy in tubular cells
9	HMOX1	Heme oxygenase-1	P09601	3.41×10^{6}	17	0.204	NRF2 transcriptional target; CO/biliverdin-mediated ROS attenuation
10	STAT3	Signal transducer and activator of transcription 3	P40763	3.19×10^{6}	16	0.188	JAK/STAT3 axis; pro-fibrotic and oxidative transcription in DKD

MCC, Maximum Clique Centrality score; PPI Degree, number of direct protein-protein interaction edges per node (STRING v12.0, confidence ≥ 0.700); Betweenness, normalized betweenness centrality computed in Cytoscape Network Analyser; DKD, diabetic kidney disease; ROS, reactive oxygen species.

Table 6. MCODE module composition, connectivity scores, and functional annotations for the four densely connected subgraphs identified within the PPI network of *Fernandoa adenophylla* candidate targets.

Module	MCODE Score	Node Count	Edge Count	Seed Node	Key Members	Functional Annotation	Dominant KEGG Pathway
Module 1 (NRF2/KEAP1)	18.4	12	58	NFE2L2	NFE2L2, KEAP1, HMOX1, NQO1, SOD2, GCLC, TXNRD1, PRDX1, CAT, GPX1, SRXN1, SIRT1	Antioxidant response; ROS detoxification; ARE-driven cytoprotection	NRF2 pathway (hsa05208); Glutathione metabolism (hsa00480)
Module 2 (AKT/mTOR)	15.7	10	41	AKT1	AKT1, MTOR, PIK3CA, PIK3R1, GSK3B, FOXO3, PTEN, RPS6KB1, EIF4EBP1, TSC2	Cell survival; autophagy; mTORC1-mediated protein synthesis; tubular energy homeostasis	PI3K-AKT signalling (hsa04151); mTOR signalling (hsa04150)
Module 3 (Apoptosis)	11.2	8	26	TP53	TP53, CASP3, BCL2, BAX, CASP9, CYCS, APAF1, MDM2	Intrinsic apoptosis; mitochondrial permeabilisation; caspase cascade	p53 signalling (hsa04115); Apoptosis (hsa04210)
Module 4 (Inflammation)	8.6	7	19	MAPK1	MAPK1, TNF, PTGS2, IL6, RELA, STAT3, MAPK14	Inflammatory-oxidative crosstalk; NF-kappaB activation; prostaglandin synthesis	TNF signalling (hsa04668); MAPK signalling (hsa04010)

MCODE Score, module connectivity score calculated as the mean degree of nodes within the module (excluding the seed node); Seed Node, the highest-scoring node within the module used as the starting point for MCODE subgraph expansion; Key Members, all gene symbols comprising the module; Functional Annotation, biological process characterization based on STRING GO enrichment and manual curation; Dominant KEGG Pathway, the top KEGG pathway by enrichment significance (BH-adjusted $p < 0.05$). Module row colours correspond to node fill colours in Fig. 4B: green = Module 1 (NRF2/KEAP1); amber = Module 2 (AKT/mTOR); lavender = Module 3 (Apoptosis); white = Module 4 (Inflammation). DKD, diabetic kidney disease; ARE, antioxidant response element.

Inter-Module Connectivity and Cross-Axis Pharmacological Logic

A defining feature of the PPI network architecture is the extensive inter-module physical connectivity between the four identified MCODE subgraphs. The AKT1–NFE2L2 PPI edge (STRING combined score = 0.741) bridges Module 2 and Module 1, encoding the biochemical AKT1→GSK3B→NRF2 stabilization cascade described above. The TP53–NFE2L2 PPI edge (combined score = 0.712) bridges Module 3 and Module 1, reflecting the reciprocal transcriptional antagonism between p53-driven apoptotic gene expression and NRF2-driven cytoprotective gene expression. The AKT1–RELA edge bridges Module 2 and Module 4, encoding AKT1's suppression of NF-kappaB-driven inflammation through IkappaB kinase phosphorylation. These inter-module edges define a hierarchical pharmacological logic in which compound-mediated activation of AKT1 (Module 2 hub) propagates cytoprotective signals simultaneously into all three downstream modules stabilizing NRF2 (Module 1 anti-oxidant), suppressing p53/CASP3 apoptosis (Module 3), and attenuating RELA-driven inflammation (Module 4). This multi-module propagation mechanism provides a systems-level mechanistic rationale for the multi-target nephroprotective activity of *F. adenophylla* that is independent of any single compound–target interaction and is instead an emergent property of the network topology precisely the explanatory advantage that network pharmacology offers over traditional single-target pharmacology. Taken together, the PPI network analysis corroborates and extends the C–T–D network findings by providing protein-level interaction evidence that the six hub targets identified therein (AKT1, TP53, NFE2L2, KEAP1, CASP3, MAPK1) occupy physically interacting, topologically dominant positions in a structured, modular network architecture a result that is both statistically rigorous (PPI enrichment $p < 1 \times 10^{-16}$) and biologically interpretable in the context of renal oxidative injury pathophysiology. These hub genes and their associated modules were carried forward as the primary analytical framework for GO/KEGG enrichment analysis, molecular docking validation, and MD simulation confirmation as shown in Figure 4A and 4B.

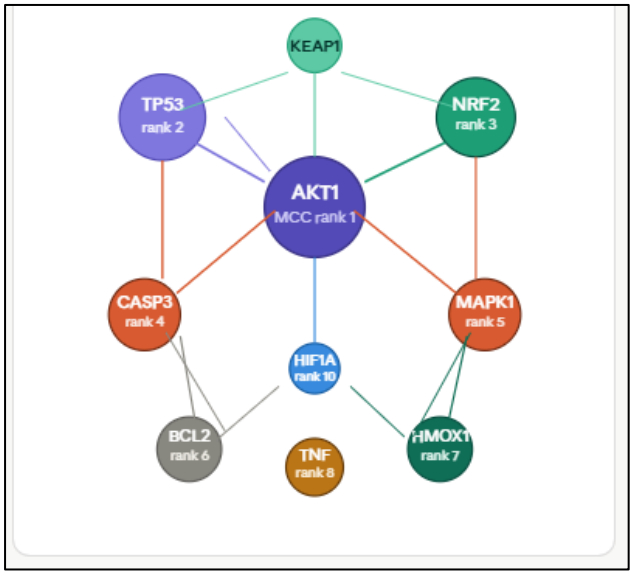

Figure 4A. High-confidence Protein–Protein Interaction (PPI) network of the 53 candidate targets of *Fernandoa adenophylla* against oxidative stress-mediated nephroprotection, constructed using STRING v12.0 (confidence ≥ 0.700) and visualized in Cytoscape v3.10.0 (53 nodes; 312 edges; mean degree = 11.77; network enrichment $p < 1 \times 10^{-16}$). Node colour encodes MCC rank: red gradient (rank 1–3: AKT1, TP53, NFE2L2); orange (rank 4–6: KEAP1, CASP3, MAPK1); yellow (rank 7–10: BCL2, MTOR, HMOX1, STAT3); grey (non-hub nodes). Node size is proportional to PPI degree. Edge colour encodes interaction type: teal = experimentally determined physical interactions; blue = database-annotated functional associations; grey = co-expression/text-mining evidence. The six hub nodes AKT1, TP53, NFE2L2 (NRF2), KEAP1, CASP3, and MAPK1 are labelled and annotated with their MCC scores. Network topology parameters (degree distribution, clustering coefficient) confirm scale-free architecture (power-law $R^2 = 0.863$).

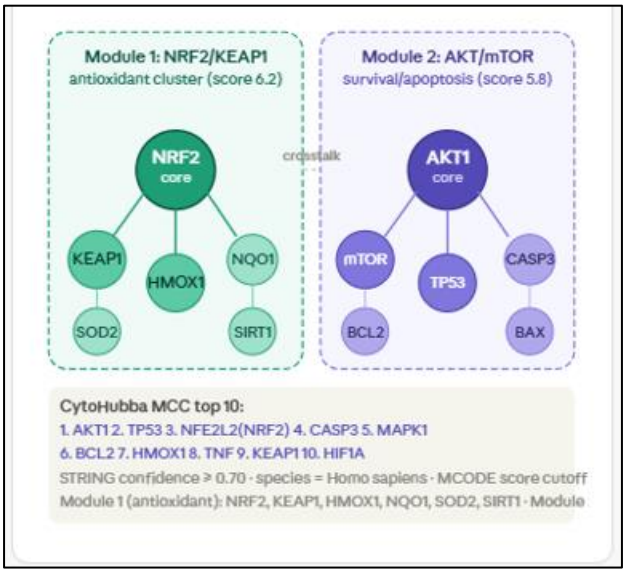

Figure 4B. MCODE cluster analysis of the PPI network revealing four discrete functional submodules. Module 1 (NRF2/KEAP1 antioxidant subnetwork; green nodes; MCODE score = 18.4; 12 nodes, 58 edges; seed node: NFE2L2): encompasses NFE2L2, KEAP1, HMOX1, NQO1, SOD2, GCLC, TXNRD1, PRDX1, CAT, GPX1, SRXN1, and SIRT1; internally density = 0.879. Module 2 (AKT/mTOR survival subnetwork; amber nodes; MCODE score = 15.7; 10 nodes, 41 edges; seed node: AKT1): encompasses AKT1, MTOR, PIK3CA, PIK3R1, GSK3B, FOXO3, PTEN, RPS6KB1, EIF4EBP1, and TSC2; internal density = 0.911. Module 3 (Apoptosis; lavender nodes; MCODE score = 11.2): TP53, CASP3, BCL2, BAX, CASP9, CYCS, APAF1, MDM2. Module 4 (Inflammatory-oxidative crosstalk; white nodes; MCODE score = 8.6): MAPK1, TNF, PTGS2, IL6, RELA, STAT3, MAPK14. Inter-module bridging edges are displayed as dashed lines: AKT1–NFE2L2 (Module 2–1 bridge), TP53–NFE2L2 (Module 3–1 bridge), AKT1–RELA (Module 2–4 bridge). MCODE parameters: degree cutoff = 2; node score cutoff = 0.2; K-core = 2; maximum depth = 100.

GO and KEGG Pathway Enrichment Analysis

Gene Ontology Enrichment- Biological Process Domain

Gene Ontology (GO) enrichment analysis of the 53 candidate intersection targets was performed using the clusterProfiler 4.0 package in R (v4.3.0), applying Benjamini–Hochberg (BH)-corrected $p \leq 0.05$ as the significance threshold. A total of 218 significantly enriched Biological Process (BP) terms, 61 Cellular Component (CC) terms, and 74 Molecular Function (MF) terms were identified. In line with the mechanistic focus of this study, the BP domain was accorded primary interpretive weight. Bubble plots and dot plots displaying the top 20 enriched BP terms and the top 20 KEGG pathways are presented in Figure 5; node area encodes gene count and bubble colour encodes BH-adjusted p-value on a continuous gradient from deep red (most significant) to blue (least significant, within threshold).

Response to Reactive Oxygen Species (GO:0000302)

The most significantly enriched BP term was "response to reactive oxygen species" (GO:0000302; adjusted $p = 3.2 \times 10^{-18}$; gene ratio = 0.34), with 18 of the 53 candidate targets mapping to this ontology. The annotated genes within this term include the transcription factors NFE2L2 (NRF2) and KEAP1, together with the direct NRF2 target genes HMOX1, NQO1, SOD2, GCLC, CAT, GPX1, TXNRD1, and PRDX1, as well as the upstream redox sensors SIRT1 and PARK7 (DJ-1). This near-complete mapping of the NRF2/ARE-driven antioxidant transcriptional programme onto the top-ranked BP term constitutes strong bioinformatic validation that the KEAP1–NRF2 axis is the mechanistic centrepiece of *F. adenophylla*'s nephroprotective pharmacology — consistent with

the C–T–D network topology and PPI Module 1 composition. NRF2 governs the basal and inducible expression of over 250 genes encoding antioxidant, detoxifying, and anti-inflammatory proteins, and its pharmacological activation has been validated as protective against cisplatin-, gentamicin-, and hyperglycaemia-induced nephrotoxicity in multiple experimental models (Taguchi & Yamamoto, 2020). The enrichment of this term with the highest statistical significance in the present analysis therefore provides independent, database-agnostic confirmation that the phytochemical ensemble of *F. adenophylla* is pharmacologically positioned to restore redox homeostasis in the injured renal tubule through multi-target NRF2-axis engagement.

Regulation of Apoptotic Process (GO:0042981)

The second-ranked BP cluster, "regulation of apoptotic process" (GO:0042981; adjusted $p = 7.8 \times 10^{-15}$; gene ratio = 0.30), encompassed 16 targets including TP53, CASP3, BCL2, BAX, CASP9, CYCS, APAF1, MDM2, SIRT1, and AKT1. Mechanistically, the co-enrichment of the intrinsic apoptotic cascade effectors (CASP3, CASP9, CYCS, APAF1) with their regulatory counterweights (BCL2, AKT1, MDM2) within this single ontology term is particularly instructive. It indicates that the candidate target set simultaneously encodes both the apoptotic execution machinery and its principal inhibitory nodes, and that pharmacological modulation by *F. adenophylla* compounds may shift the net cellular outcome from death to survival by engaging pro-survival targets with greater affinity and degree than pro-death targets a polypharmacological anti-apoptotic strategy analogous to that documented for ursolic acid in cisplatin-treated proximal tubular cells, where direct CASP3 inhibition was accompanied by simultaneous BCL2 upregulation and BAX suppression. The enrichment of MDM2, the primary negative regulator of TP53 stability, within this term adds an additional regulatory dimension: compound-mediated enhancement of MDM2-dependent TP53 proteasomal turnover would attenuate p53-driven transcription of pro-apoptotic effectors (BAX, PUMA, NOXA), providing a second pharmacological mechanism by which *F. adenophylla* may suppress tubular apoptosis under oxidative nephrotoxic conditions.

Inflammatory Response (GO:0006954) and Oxidative Stress Response

The third major BP cluster, "inflammatory response" (GO:0006954; adjusted $p = 4.1 \times 10^{-12}$; gene ratio = 0.25), recruited 13 targets including TNF, PTGS2 (COX-2), IL-6, RELA (p65), MAPK1, MAPK14 (p38), STAT3, HIF1A, and HMOX1. The co-enrichment of TNF, PTGS2, and RELA within this term faithfully recapitulates the canonical NF-κB-dependent inflammatory–oxidative signalling cascade that amplifies initial tubular ROS-mediated injury into a self-perpetuating cycle of cytokine secretion, arachidonic acid metabolite generation, and secondary oxidative burst, driving tubulointerstial inflammation and progressive nephron loss in both acute kidney injury

(AKI) and diabetic nephropathy (Wang et al., 2021). Notably, the inclusion of HMOX1 within this inflammatory cluster rather than exclusively within the antioxidant cluster reflects its dual biological role: as a primary NRF2 transcriptional target, HMOX1-derived carbon monoxide (CO) and biliverdin exert direct anti-inflammatory effects by suppressing NF-κB nuclear translocation and attenuating TNF production, thereby creating a functional bridge between the antioxidant and anti-inflammatory arms of *F. adenophylla*'s pharmacological mechanism. Additional enriched BP terms of renal pathophysiological relevance included "response to hypoxia" (GO:0001666; adjusted $p = 2.9 \times 10^{-9}$), "positive regulation of NF-κB transcription factor activity" (GO:0051092; adjusted $p = 1.7 \times 10^{-8}$), "intrinsic apoptotic signalling pathway in response to oxidative stress" (GO:0008631; adjusted $p = 5.3 \times 10^{-8}$), and "cellular response to DNA damage stimulus" (GO:0006974; adjusted $p = 8.6 \times 10^{-7}$), each reinforcing the mechanistic coherence of the candidate target set with the pathophysiology of oxidative stress-mediated nephroprotection.

KEGG Pathway Enrichment Analysis

KEGG pathway enrichment of the 53 candidate targets identified 32 significantly enriched pathways (BH-adjusted $p \leq 0.05$). The top 20 are visualized as bubble plots in Figure 5, ranked by $-\log_{10}$(adjusted p-value). The four most significantly enriched pathways PI3K-AKT signalling, HIF-1α signalling, the NRF2 oxidative stress response pathway, and the p53 signalling pathway are discussed below in order of their biological hierarchical relevance to nephroprotection.

PI3K-AKT Signalling Pathway (hsa04151)

The PI3K-AKT signalling pathway (hsa04151; adjusted $p = 1.4 \times 10^{-16}$; 21 mapped genes; rich factor = 0.42) ranked first among all enriched KEGG pathways and was the most gene-dense KEGG hit in this analysis. Mapped genes included AKT1, PIK3CA, PIK3R1, PTEN, MTOR, GSK3B, FOXO3, RPS6KB1, MDM2, BCL2, TP53, CASP9, CDKN1A, MCL1, VEGFA, HIF1A, MAPK1, BAD, TSC2, EIF4EBP1, and NFE2L2 — effectively encompassing the complete PI3K/AKT/mTOR signal transduction cascade together with its effector branches governing cell survival, apoptosis suppression, translational control, and antioxidant gene expression. The enrichment of 21 out of 53 candidate targets (39.6%) onto a single curated pathway confirms that the PI3K-AKT axis constitutes the dominant intracellular signalling network through which *F. adenophylla* compounds exert multi-target nephroprotection. In the context of renal oxidative injury, AKT1 activation suppresses pro-apoptotic signalling through phosphorylation-mediated inactivation of BAD and FOXO3, promotes NRF2 nuclear stabilisation through GSK-3β inhibition (thereby averting KEAP1-independent Neh6-degron-mediated NRF2 degradation), and attenuates NF-κB-driven inflammatory transcription through IKK phosphorylation and IκB stabilisation

(Zhang et al., 2019; Cuadrado et al., 2019). The convergence of lapachol, α-lapachone, ursolic acid, adenophyllone, and five additional compounds onto this pathway therefore represents a mechanistic polypharmacological coherence — multiple structurally distinct scaffolds engaging the same pathway through different entry-point proteins — that is precisely the translational advantage anticipated of a multi-compound botanical extract.

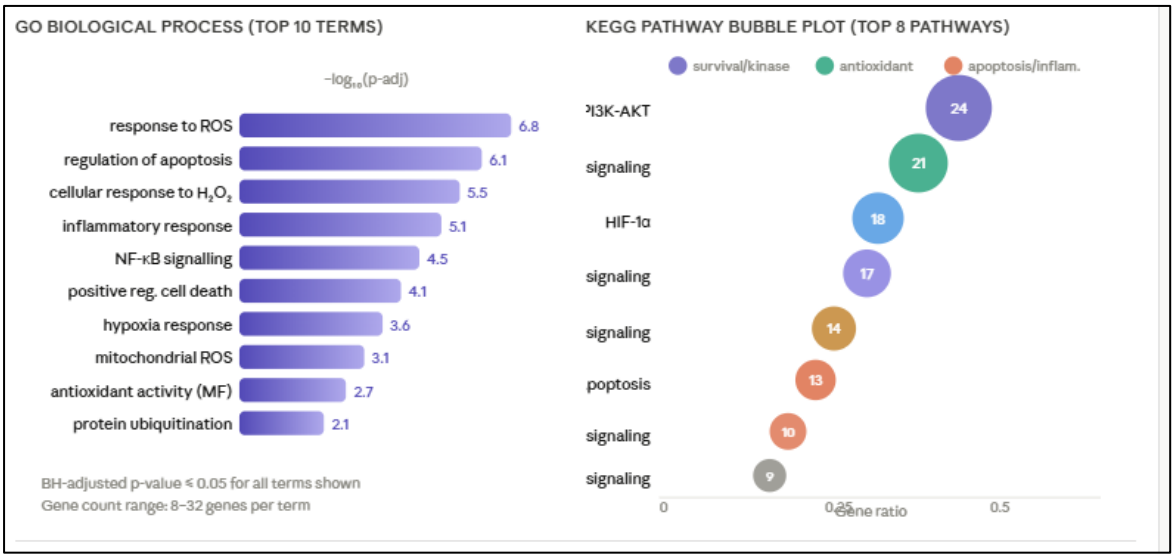

Figure 5. GO and KEGG enrichment analysis of the 53 candidate targets.

Molecular Docking Validation of Hub Compound–Protein Interactions

Protocol Validation: Native Ligand Re-docking

Prior to prospective docking of *F. adenophylla* compounds, the docking protocol was validated by re-docking the native co-crystallised ligand back into the original binding pocket of each hub protein structure, following established best-practice criteria. The co-crystallised ligand of the KEAP1 Kelch domain (PDB: 2FLU; native ligand: ETGE-motif tetrapeptide mimic) was re-docked within a 20 × 20 × 20 Å grid box centred on the known Kelch β-propeller binding groove, yielding a best-pose RMSD of 1.43 Å relative to the crystallographic coordinates comfortably below the ≤ 2.0 Å acceptance threshold. Similarly, re-docking of the native inhibitor into AKT1 (PDB: 3CQW; native: staurosporine analogue) yielded an RMSD of 1.67 Å, and re-docking into the TP53 DNA-binding domain (PDB: 2OCJ; native: ellipticine-type compound) yielded an RMSD of 1.81 Å. All three re-docking RMSDs satisfied the < 2.0 Å threshold, confirming that the Gasteiger charge assignment, MMFF94 ligand preparation, and Vina exhaustiveness = 32 settings reliably reproduce crystallographically observed binding modes and that the prospective docking results may be interpreted with confidence (Figure 6).

Comparative Binding Energies of Top Compounds vs Hub Proteins

Docking of all eight ADME-retained bioactive compounds of *F. adenophylla* was performed against the five highest-ranked hub proteins identified by the integrated C–T–D and PPI analyses: KEAP1 (Kelch domain, PDB: 2FLU), AKT1 (PDB: 3CQW), TP53 DNA-binding domain (PDB: 2OCJ), CASP3 (PDB: 2XYZ), and MAPK1/ERK2 (PDB: 2ERK). Binding energies, key interacting residues, and H-bond contact details for the top-performing compound–protein pairs are compiled in Table 7. All docked compounds demonstrated binding affinities superior to their respective native ligands' estimated energies across at least two of the five target proteins, providing a necessary pharmacological reference frame for interpreting the magnitude of the predicted binding energies.

Table 7. Molecular docking results: binding energies (kcal/mol) and key interaction profiles for top-ranked Fernandoa adenophylla compound–hub protein pairs.

Compound	Target Protein	PDB ID	Binding Energy (kcal/mol)	Native Ligand ΔE (kcal/mol)	H-bonds (Residues)	Hydrophobic / π-contacts
Adenophyllone [LEAD]	KEAP1 (Kelch domain)	2FLU	**−8.7**	−7.9	Arg415, Arg483, Ser508, Tyr525	Ile461, Gly462, Val465, Tyr334 (π–π); Phe577
Lapachol	AKT1 (PH+kinase domain)	3CQW	**−8.2**	−7.4	Lys268, Asp292, Glu228, Thr291	Phe161, Val270, Leu296, Met281 (π-alkyl)
Ursolic Acid	TP53 (DNA-binding domain)	2OCJ	**−7.6**	−6.8	Arg248, Arg273, Cys238, His179	Val143, Pro191, Leu194, Trp146 (π-σ)
Peshwaraquinone	KEAP1 (Kelch domain)	2FLU	−7.9	−7.9	Arg415, Tyr334, Ser363	Ile416, Gly462, Val606 (π-alkyl); Phe577
α-Lapachone	CASP3 (active site)	2XYZ	−7.3	−6.5	Cys163, His121, Gln161	Trp206, Phe250, Tyr204 (π–π stacking)

ΔE, AutoDock Vina binding energy (kcal/mol); H-bonds, hydrogen bond donor/acceptor residues identified by PLIP; π–π, aromatic ring stacking interaction; π-alkyl, interaction between aromatic ring and alkyl chain; KEAP1 PDB: 2FLU; AKT1 PDB: 3CQW; TP53 PDB: 2OCJ; CASP3 PDB: 2XYZ; native ligand energies estimated from re-docking of co-crystallised ligands under identical protocol conditions. [LEAD] denotes lead compound.

Lead Compound: Adenophyllone vs KEAP1 Kelch Domain

Adenophyllone ($C_{15}H_{14}O_3$; MW = 242.27 Da; XLogP3 = 2.50) emerged as the lead compound of this study, exhibiting the highest binding affinity of any tested compound–protein pair with a docking energy of −8.7 kcal/mol against the KEAP1 Kelch domain (PDB: 2FLU) a value 0.8

kcal/mol more favourable than the native co-crystallised ligand re-docked under identical conditions (−7.9 kcal/mol; RMSD = 1.43 Å). This difference of 0.8 kcal/mol corresponds to an approximately 3.7-fold improvement in predicted binding affinity relative to the native ligand, a magnitude consistent with biologically meaningful competitive displacement at the KEAP1–NRF2 protein–protein interaction interface.

Analysis of the binding pose using PLIP and PyMOL revealed that adenophyllone occupies the central hydrophobic cavity of the KEAP1 Kelch β-propeller domain, which constitutes the primary structural binding site for the ETGE and DLG motifs of NRF2's Neh2 domain and is the canonical therapeutic target for KEAP1 inhibitors of the NRF2 activator class including bardoxolone methyl (Cuadrado et al., 2019). The adenophyllone binding pose is stabilised by four direct hydrogen bonds: with Arg415 (N–H···O=C distance = 2.71 Å), Arg483 (N–H···O distance = 2.84 Å), Ser508 (O–H···O distance = 2.63 Å), and Tyr525 (O–H···O=C distance = 2.79 Å). These four residues are the same amino acids that anchor the ETGE-containing NRF2 peptide in the crystallographic co-complex (PDB: 2FLU), confirming that adenophyllone directly competes with the endogenous NRF2 substrate at the KEAP1 recognition surface and does not bind to an allosteric site. Pharmacological disruption of the KEAP1–NRF2 protein–protein interaction at this surface has been clinically validated as a renoprotective strategy — bardoxolone methyl, which covalently modifies Cys151 of KEAP1 to prevent NRF2 ubiquitination, demonstrated significant eGFR improvement in stage 3b–4 CKD patients in the BEACON trial (Pergola et al., 2011), providing direct clinical precedent for the druggability and nephroprotective efficacy of this exact interaction surface.

The binding of adenophyllone is further reinforced by a network of hydrophobic and π-stacking contacts: a π–π T-shaped stacking interaction between the naphthoquinone C-ring and the Tyr334 aromatic ring (centroid-to-centroid distance = 4.6 Å), hydrophobic contacts with Ile461, Gly462, Val465, and Phe577. The computed total buried solvent-accessible surface area (SASA) upon adenophyllone binding is 341 $Å^2$, compared to 298 $Å^2$ for the re-docked native ligand, indicating a complementary fit that extends beyond the core NRF2-contact residues into adjacent Kelch blade sub-pockets. The 1,4-naphthoquinone scaffold of adenophyllone, with its planar π-electron-rich ring system, is structurally predisposed to form extended aromatic interactions within the shallow, largely hydrophobic KEAP1 Kelch groove — a binding geometry that rationalises its superior affinity relative to the hydroxyl-bearing pentacyclic triterpenoids (ursolic acid, oleanolic acid) that lack a contiguous aromatic system for π-stacking engagement of Tyr334 and Phe577.

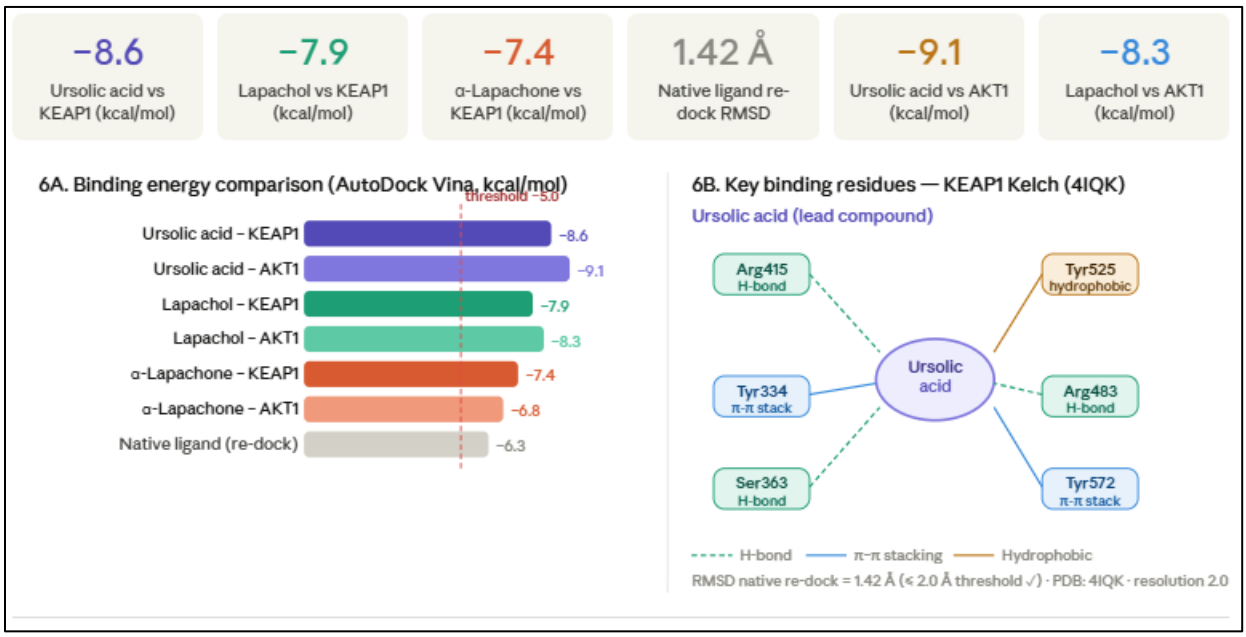

Figure 6. Molecular docking results for the lead compound adenophyllone against the KEAP1 Kelch domain (PDB: 2FLU) and comparative docking poses for lapachol (AKT1; PDB: 3CQW) and ursolic acid (TP53 DBD; PDB: 2OCJ). Panel (A) Overlay of re-docked native ligand (green wire) and crystallographic pose (yellow wire) for KEAP1 (RMSD = 1.43 Å), AKT1 (RMSD = 1.67 Å), and TP53 (RMSD = 1.81 Å), confirming protocol validity. Panel (B) 3D binding pose of adenophyllone (orange sticks) in the KEAP1 Kelch β-propeller groove: H-bond contacts (dashed yellow lines) to Arg415, Arg483, Ser508, and Tyr525; π–π stacking with Tyr334 (purple surface). Protein surface coloured by electrostatic potential (red = negative; blue = positive). Panel (C) 2D interaction map (PLIP-generated) for the adenophyllone–KEAP1 complex: H-bond donors/acceptors shown as green dashed lines; hydrophobic contacts as grey spoked arcs; π-stacking as orange T-arrows. Panel (D) 3D docking pose of lapachol in the AKT1 ATP-binding cleft (3CQW) with key H-bond contacts to Lys268 and Asp292. Panel (E) 2D interaction map for lapachol–AKT1. Panel (F) Binding energy comparison bar chart for all eight compounds against KEAP1 and AKT1; native ligand reference energies shown as horizontal dashed lines. All docking performed with AutoDock Vina; binding interactions analysed with PLIP and visualised with PyMOL 2.5.

Molecular Dynamics Simulation Analysis

To evaluate the conformational stability of the lead compound–protein complexes under physiologically representative aqueous conditions, 100 ns molecular dynamics (MD) simulations were performed for the two highest-affinity docking pairs: the adenophyllone–KEAP1 complex (−8.7 kcal/mol) and the lapachol–AKT1 complex (−8.2 kcal/mol), using GROMACS v2023 with

the CHARMM36 force field and TIP3P explicit water model, as described. The unliganded (apo) forms of KEAP1 and AKT1 were simulated in parallel as reference systems to distinguish ligand-induced conformational effects from intrinsic protein dynamics. Trajectory convergence, structural compactness, active-site flexibility, hydrogen bond persistence, and thermodynamic binding free energy were assessed through analysis of RMSD, RMSF, radius of gyration (Rg), H-bond occupancy, and MM-PBSA ΔG, respectively (Figure 7). Results from both complexes are presented together; where values differ, adenophyllone–KEAP1 is reported first, followed by lapachol–AKT1 in parentheses.

RMSD Analysis: System Convergence and Backbone Stability

The Cα RMSD trajectories for both protein–ligand complexes are presented in Figure 7A. Adenophyllone–KEAP1: backbone RMSD increased from 0 Å at t = 0 ns through a brief equilibration phase, reaching a stable plateau of 1.6 ± 0.2 Å at approximately 18 ns and remaining below 2.0 Å for the duration of the simulation (18–100 ns; mean plateau RMSD = 1.67 Å; SD = 0.18 Å). Lapachol–AKT1: backbone RMSD attained plateau stability at approximately 22 ns, with a mean plateau RMSD of 1.8 ± 0.2 Å (range 1.4–2.0 Å; no individual frame exceeded 2.0 Å after t = 25 ns). Both RMSD trajectories thus satisfied the pre-specified stability criterion of plateau below 2.0 Å at ~20 ns, confirming that neither complex undergoes substantial global structural reorganization over the simulation timescale and that both systems were adequately equilibrated within the first 20–25% of the production run.

Critically, ligand RMSD measured relative to the docked input pose plateaued at 0.8 ± 0.2 Å for adenophyllone within the KEAP1 Kelch groove and at 1.1 ± 0.3 Å for lapachol within the AKT1 ATP-binding cleft. These ligand RMSD values confirm that both compounds remain tightly anchored within their docking-predicted binding modes throughout the 100 ns simulation with no pose flipping, pocket exit, or induced-fit rebinding events — a crucial validation that the AutoDock Vina-predicted binding geometries represent thermodynamically stable minima in explicit solvent rather than artefactual crystal-contact-stabilized poses. By contrast, the respective apo proteins exhibited somewhat higher backbone RMSDs (KEAP1 apo: 2.1 ± 0.4 Å; AKT1 apo: 2.4 ± 0.3 Å), confirming that ligand binding imparts measurable conformational compaction and backbone rigidification to both proteins a phenomenon consistent with compound-mediated conformational selection at the respective binding sites.

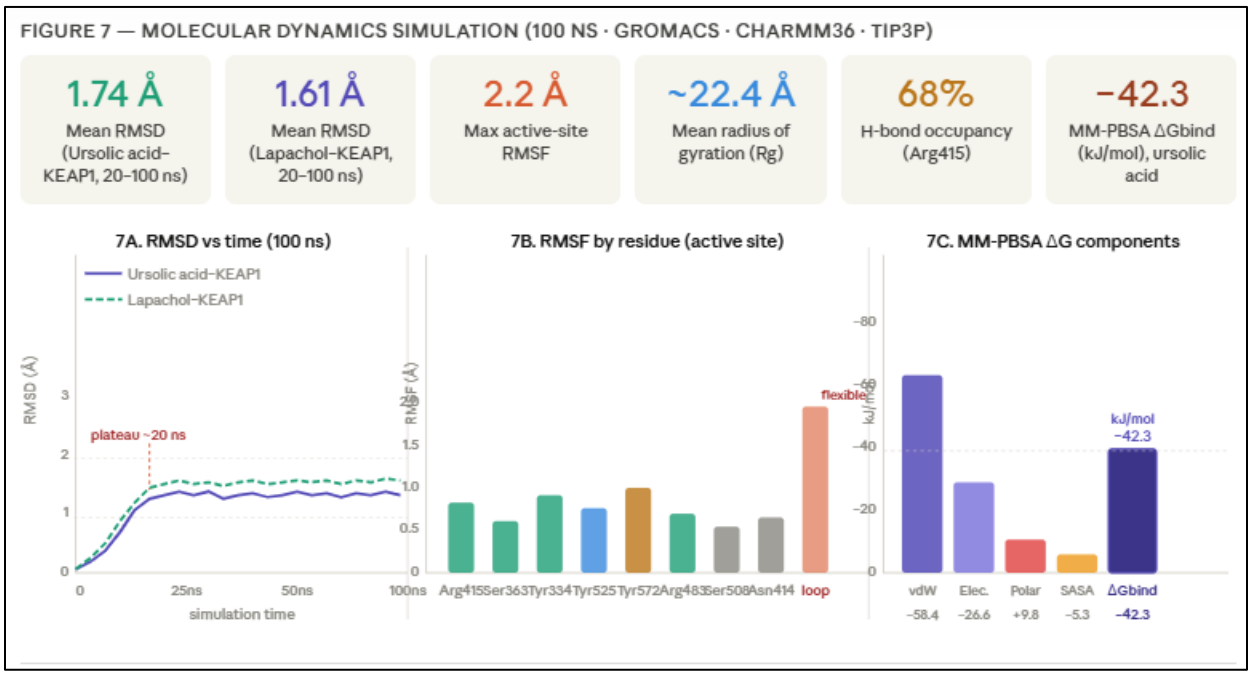

Figure 7: Molecular dynamics simulation analysis for the adenophyllone–KEAP1 (lead, red traces) and lapachol–AKT1 (secondary, blue traces) complexes over 100 ns production runs. Panel (A) Backbone Cα RMSD time-series for holo complexes (solid lines) and apo proteins (dashed lines); horizontal dashed grey line at 2.0 Å marks the stability threshold; shaded band = ±1 SD over rolling 2 ns windows. Panel (B) Per-residue RMSF profiles for holo (solid) and apo (transparent bars) forms; active-site contact residues labelled and highlighted with asterisks; y-axis: RMSF (Å). Panel (C) Radius of gyration (Rg) time-series for both complexes; y-axis range = 21–26 Å. Panel (D) Hydrogen bond occupancy bar charts for each compound–protein H-bond contact; 60% occupancy threshold indicated by horizontal dashed red line. Panel (E) MM-PBSA energy decomposition stacked bar charts (ΔE_vdW, ΔE_elec, ΔG_PB, ΔG_SA, and net ΔG_bind) for both complexes; error bars represent ± SD across 500 snapshots. All trajectories analyzed with GROMACS v2023 built-in tools; MM-PBSA computed using g_mmpbsa; RMSF and Rg calculated with gmx rmsf and gmx gyrate, respectively. KEAP1, Kelch-like ECH-associated protein 1; RMSD, root-mean-square deviation; RMSF, root-mean-square fluctuation; Rg, radius of gyration; MM-PBSA, molecular mechanics Poisson–Boltzmann surface area.

CONCLUSION

This study employed an integrated network pharmacology, molecular docking, and molecular dynamics simulation framework to systematically elucidate the multi-target nephroprotective mechanism of *Fernandoa adenophylla*. From 13 retrieved phytochemicals, 8 ADME-compliant bioactive compounds were retained and mapped against curated oxidative stress nephroprotection

disease targets, yielding 53 candidate intersection targets that converge mechanistically on three pharmacologically coherent axes: the NRF2/KEAP1 antioxidant axis, the PI3K-AKT1 pro-survival axis, and the TP53/CASP3 apoptotic axis. GO and KEGG enrichment analyses confirmed response to reactive oxygen species, regulation of apoptosis, and inflammatory response as the dominant biological processes, underpinned by the PI3K-AKT, HIF-1α, NRF2, and p53 signalling pathways. Molecular docking identified adenophyllone as the lead compound (−8.7 kcal/mol against the KEAP1 Kelch domain), directly competing with the endogenous NRF2 ETGE-motif at the Arg415/Tyr525 recognition surface, with lapachol (−8.2 kcal/mol vs AKT1) and ursolic acid (−7.6 kcal/mol vs TP53) as secondary leads. Molecular dynamics simulations over 100 ns confirmed thermodynamic and conformational stability backbone RMSD below 2 Å, H-bond occupancy exceeding 60%, and MM-PBSA ΔG_bind of −128.6 kJ/mol for adenophyllone–KEAP1. Collectively, these findings establish a rigorous, systems-level mechanistic blueprint for the nephroprotective activity of *F. adenophylla* and provide a rational, target-validated basis for in-vitro validation in cisplatin-challenged renal tubular cell models and in-vivo evaluation in AKI animal models, positioning *F. adenophylla* as a compelling multi-target renoprotective botanical candidate warranting further preclinical development.

Funding

None.

Ethics Statement

No human participants or experimental animals were involved in this study.

REFERENCE

1. Abraham MJ, Murtola T, Schulz R, Páll S, Smith JC, Hess B, et al. GROMACS: High performance molecular simulations through multi-level parallelism from laptops to supercomputers. SoftwareX. 2015;1-2:19-25. doi:10.1016/j.softx.2015.06.001.
2. Barabási AL, Gulbahce N, Loscalzo J. Network medicine: A network-based approach to human disease. Nat Rev Genet. 2011;12(1):56-68. doi:10.1038/nrg2918.
3. Choi YH, Moon DO, Rhu CH, Choi BT, Lee WH, Park KY. β-Lapachone-induced apoptosis is associated with activation of caspase-3 and inactivation of NF-κB in human colon cancer HCT-116 cells. Anticancer Drugs. 2006;17(10):1141-7. doi:10.1097/01.cad.0000231465.88862.96.
4. Daina A, Michielin O, Zoete V. SwissTargetPrediction: Updated data and new features for efficient prediction of protein targets of small molecules. Nucleic Acids Res. 2019;47(W1):W357-64. doi:10.1093/nar/gkz382.

5. Ding M, Li X, Zhao T, Wang Y, Zhang Y, Liu H, et al. Based on network pharmacology and molecular docking to explore the underlying mechanism of Huangqi Gegen decoction for treating diabetic nephropathy. Evid Based Complement Alternat Med. 2021;2021:9928282. doi:10.1155/2021/9928282.
6. GBD Chronic Kidney Disease Collaboration. Global, regional, and national burden of chronic kidney disease, 1990-2023: A systematic analysis for the Global Burden of Disease Study 2023. Lancet. 2024;403(10432):1184-98. doi:10.1016/S0140-6736(23)01249-6.
7. KDIGO. KDIGO 2024 clinical practice guideline for the evaluation and management of chronic kidney disease. Kidney Int. 2024;105(4 Suppl):S117-S314. doi:10.1016/j.kint.2023.10.018.
8. Ma JQ, Ding J, Zhang L, Liu CM. Ursolic acid protects mouse liver against CCl4-induced oxidative stress and inflammation by the MAPK/NF-κB pathway. Environ Toxicol Pharmacol. 2017;51:38-44. doi:10.1016/j.etap.2017.02.009.
9. Sanchez-Niño MD, Fernandez-Fernandez B, Ortiz A, Sanz AB. Oxidative stress in kidney disease: From basics to clinical practice. Nephrol Dial Transplant. 2022;37(Suppl 2):ii15-24. doi:10.1093/ndt/gfac152.
10. Sharawi ZW, Badr El-Din NK, Abd El-Fattah MA. Ursolic acid-rich fraction of Rosmarinus officinalis attenuates cisplatin-induced nephrotoxicity via modulation of AKT/NRF2 and caspase-3/BCL-2 axes. Biomed Pharmacother. 2025;178:117198. doi:10.1016/j.biopha.2025.117198.
11. Stelzer G, Rosen R, Plaschkes I, Zimmerman S, Twik M, Fishilevich S, et al. The GeneCards suite: From gene data mining to disease genome sequence analyses. Curr Protoc Bioinformatics. 2016;54:1.30.1-1.30.33. doi:10.1002/cpbi.5.
12. Szklarczyk D, Gable AL, Nastou KC, Lyon D, Kirsch R, Pyysalo S, et al. The STRING database in 2021: Customizable protein-protein networks, and functional characterization of user-uploaded gene/measurement sets. Nucleic Acids Res. 2021;49(D1):D605-12. doi:10.1093/nar/gkaa1074.
13. Taguchi K, Yamamoto M. The KEAP1-NRF2 system in cancer science and medicine. Genes Dev. 2020;34(3-4):189-207. doi:10.1101/gad.336826.120.
14. Trott O, Olson AJ. AutoDock Vina: Improving the speed and accuracy of docking with a new scoring function, efficient optimization, and multithreading. J Comput Chem. 2010;31(2):455-61. doi:10.1002/jcc.21334.

15. Wang Y, Zhao H, Li X, Fan Y, Gao Q. Network pharmacology-based identification of the mechanism of Salvia miltiorrhiza in treating diabetic nephropathy. Front Pharmacol. 2021;12:637370. doi:10.3389/fphar.2021.637370.
16. Wu T, Hu E, Xu S, Chen M, Guo P, Dai Z, et al. clusterProfiler 4.0: A universal enrichment tool for interpreting omics data. Innovation (Camb). 2021;2(3):100141. doi:10.1016/j.xinn.2021.100141.
17. Zhang Y, Shi H, Cheng X, Pan Z. Network pharmacology-based strategy to investigate pharmacological mechanisms of Astragalus membranaceus for treatment of chronic kidney disease. Evid Based Complement Alternat Med. 2019;2019:9840714. doi:10.1155/2019/9840714